

# QUASI-MEDIAL DISTANCE FIELD (Q-MDF): A ROBUST METHOD FOR APPROXIMATING AND DISCRETIZING NEURAL MEDIAL AXIS

A PREPRINT

**Jiayi Kong\***

S-Lab

Nanyang Technological University  
Singapore

**Chen Zong\***

S-Lab

Nanyang Technological University  
Singapore

**Jun Luo**

College of Computing and Data Science  
Nanyang Technological University  
Singapore

**Shiqing Xin**

School of Computer Science  
Shandong University  
China

**Fei Hou**

Institute of Software  
Chinese Academy of Sciences  
China

**Hanqing Jiang**

SenseTime Research  
China

**Chen Qian**

SenseTime Research  
China

**Ying He<sup>†</sup>**

S-Lab

Nanyang Technological University  
Singapore

## Abstract

The medial axis, a lower-dimensional shape descriptor, plays an important role in the field of digital geometry processing. Despite its importance, robust computation of the medial axis transform from diverse inputs, especially point cloud with defects, remains a significant challenge. In this paper, we tackle the challenge by proposing a new implicit method that diverges from mainstream explicit medial axis computation techniques. Our key technical insight is the difference between the signed distance field (SDF) and the medial field (MF) of a solid shape is the unsigned distance field (UDF) of the shape's medial axis. This allows for formulating medial axis computation as an implicit reconstruction problem. Utilizing a modified double covering method, we extract the medial axis as the zero level-set of the UDF. Extensive experiments show that our method has enhanced accuracy and robustness in learning compact medial axis transform from thorny meshes and point clouds compared to existing methods.

## 1 Introduction

The medial axis [Blum(1967)] is a classical geometric structure that encapsulates both the local symmetries and global topological characteristics of a shape. When augmented with radius information, known as the medial axis transform (MAT), it enables the reconstruction of the original shape and serves as an essential lower-dimensional shape descriptor. The medial axis finds extensive applications across various domains of digital geometric processing, including shape synthesis and design [Tang et al.(2019), Petrov et al.(2024), Noma et al.(2024)], shape decomposition [Zhou et al.(2015), Lin et al.(2020)], pose analysis [Yang et al.(2021), Dou et al.(2023)], and animation [Yang et al.(2018), Lan et al.(2020), Lan et al.(2021)].

As a method of shape representation, the medial axis is centrally located, effectively capturing the protrusions and components of a shape. Topologically, the medial axis is homotopy equivalent to the solid shape. Despite these advantages, the medial axis is not a stable structure. Even slight perturbations on the boundary can introduce additional branches, as Fig. 2 (c) depicted, increasing its complexity and complicating its use in downstream applications. Additionally, the input data is not always a watertight mesh surface or densely sampled. It is common to encounter point clouds with defects such as non-uniformity, noise, or partially missing regions, which increases the difficulty of inferring a plausible original shape. Therefore, although the medial axis is rigorously defined, robustly computing a compact medial axis remains a challenge.

Most existing traditional medial axis computation techniques rely on discretization of the shape or medial axis, such as voxelization or obtaining the medial points [Saha et al.(2016), Tagliasacchi et al.(2016)]. Voxel-based approaches involve identifying a subset of a voxelized shape that aligns with the medial axis criteria. These methods are straightforward and efficient, but their accuracy is often limited by the resolution, which also affects scalability. Medial point-driven approaches utilize a collection of medial axis points, along with their connectivity, to represent the medial axis. Traditional techniques often simplify subsets of the Voronoi diagram (derived from surface sampling) to achieve a compact medial axis that balances between compactness and reconstruction accuracy. Others compute the medial axis points according to the symmetric properties of surface points, then connect them to form a medial mesh. Typically, most discretization-based approaches require high-quality inputs (e.g., watertight meshes or densely sampled points without noise), and often lead to suboptimal results when these conditions are not met.

Recently, learning-based methods have gained popularity, due to their reduced input requirements. However, these methods face challenges with limited generalization capability and often compromise the centering property and topological correctness.

\*J. Kong and C. Zong contribute equally to the project.

<sup>†</sup>Corresponding author: Y. He (yhe@ntu.edu.sg)

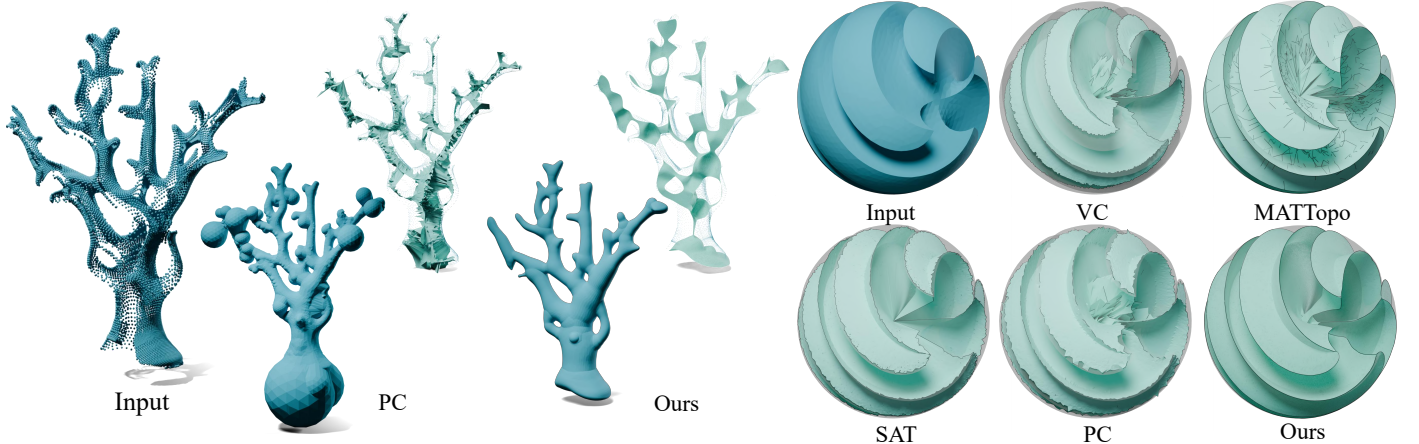


Figure 1: In this paper, we introduce a novel approach for medial axis approximation, utilizing a differentiable field, Q-MDF, to encode the medial axis and extract the medial mesh from this representation. Compared to existing methods such as PC [Amenta et al.(2001)], VC [Yan et al.(2018)], MATTopo [Wang et al.(2024b)], and SAT [Miklos et al.(2010)], our method demonstrates enhanced robustness of computing compact medial axis across a wide range of inputs. Left: The coral model exhibits partial missing data and non-uniform point distribution, which challenge typical PC, resulting in an off-centered medial axis. Consequently, surface reconstructed from it is easy to suffer topology and geometry issues. Our method, however, tolerates these issues well, producing a more stable medial axis and a cleaner reconstructed surface. Right: A sphere-like mesh input with sharp features, along with the corresponding medial axes outputs from five methods. The boundaries are visualized in black. Compared with PC, SAT, VC and MATTopo, our method could report a more compact outcome while preserving these sharp features.

Different from previous work, [Rebain et al.(2021)] considers the medial axis as a continuous differential field, referred to as the medial field. They design a comprehensive network architecture to joint train the signed distance field and correlated deep medial field simultaneously, and leverage the learned medial field to accelerate ray-surface intersection computations. However, the medial field only captures the radius information of the projected point, making it difficult to extract the medial axis from it directly.

Inspired by [Rebain et al.(2021)], we propose a novel differentiable representation of the medial axis, from which we can robustly derive a compact medial mesh. Our method begins with a key insight that for a given solid shape, its distance field of surface and medial field have strong connections. By taking the difference, we can obtain a differentiable continuous representation that is similar to an unsigned distance field of the medial axis. Then, extracting a non-manifold curved surface from its unsigned distance field is notoriously difficult. Inspired by [Hou et al.(2023)], we use the double cover technique to capture the structure of the medial axis, essentially creating a two-layered enclosure. By collapsing the volume of this enclosure to zero, we obtain a compact medial mesh that represents the medial surface. In addition, due to the feature-directed nature of the medial axis, we have further enhanced its differentiable representation for sharp features, making the extracted medial axis more precise and refined.

It is worth noting that, the joint training of signed distance field and medial field significantly expands the application range of our method, allowing for the computation of simplified medial axes in various tricky scenarios. It also provides a new perspective on shape representation and medial axis computation. Our contributions are four-fold.

- Different from the previous discrete medial axis computation approach, we developed a novel medial axis

transform approximation method, which takes thorny data as input and robustly generates a compact medial axis transform that is plausible to represent the shape.

- Based on the insight of the relationship between SDF and MF, we propose a differential representation of the medial axis.
- By utilizing the concept of double coverage, we developed an algorithm to accurately extract a medial mesh from this differential medial axis representation.
- To better handle the sharp feature of the original shape, we further enhance the relative field at this region, according to the "pointing to convex feature" property of the medial axis.

## 2 Related Work

The medial axis problem has been extensively studied over the past few decades, resulting in a large body of literature. Due to the space limitations, this section reviews only the most recent and relevant methods. For a more comprehensive literature review, we refer readers to [Tagliasacchi et al.(2016)].

### 2.1 Traditional Approaches

**Analytical Approaches** Analytical approach aims to compute accurate medial axis following its mathematical definition. One classic idea begins with the analysis of localized shape boundary, tracing seam curves and identifying junction points to construct the medial axis. Such as [Culver et al.(2004), Milenkovic(1993), Sherbrooke et al.(1996), Culver et al.(1999)] (designed for polyhedron) and [Ramanathan and Gurumoorthy(2010)] (designed for simple free-form shape). Due to the high requirement for the simplicity of input models in these methods, this greatly limits their practical use.

**Voxel-based Approaches** Most voxel-based approach discretizes the target shape to a voxel representation, and finds a subset that meets the requirement of the medial axis (e.g. thinness, centrality, homotopy equivalence), following certain distance measurements [Saha et al.(2016)]. For instance, Manhattan distance [Palágyi and Kuba(1999)], chamfer distance [Pudney(1998)] and Euclidean distance [Hesselink and Roerdink(2008), Rumpf and Telea(2002)]. Furthermore, [Yan et al.(2018)] provides a rigorous sampling condition with the help of voxel representation, and takes the dual of interior Delaunay triangulation as medial mesh, which is theoretically guaranteed to be topologically equivalence with the original shape.

**Approximation with Paired Points** This method begins with a set of oriented surface points, approximating the medial points as the center of locally maximum inscribed spheres [Ma et al.(2012)]. The connectionship between the medial points can be established through localized plane fitting [Jalba et al.(2012)]. This approach aims to provide a rough medial description of the original shape and pay less attention to geometric accuracy and topological correctness.

**Voronoi-guided Approaches** The Voronoi diagram has played a significant role in medial axis computation in recent decades, due to its special spatial partition property and computational efficiency. The following will review typical algorithms that compute the medial axis using Voronoi diagrams.

It has been proved that in  $\mathbb{R}^2$ , if it meets  $\epsilon$ -sampling on the boundary curve, the subset of Voronoi diagram that is completely contained in the shape approximates the medial axis [Brandt(1994)]. However, this cannot be directly extended to the 3D scenario due to the presence of “slivers”, which can produce Voronoi vertices that are close to the surface and lead to redundant branches [Amenta et al.(2001)]. Therefore, a large number of works have been dedicated to removing redundant branches caused by these abnormal points from this subcomplex. [Attali and Montanvert(1996), Dey and Zhao(2004)] prune the Voronoi diagram by applying the angle criterion, while there is no guarantee that the topology could be efficiently preserved at this procedure. [Giesen et al.(2006)] further enhanced topological correctness using the unstable manifold of the Voronoi diagram. [Chazal and Lieutier(2005), Chazal and Lieutier(2008)] employ a radius criterion to prune this subcomplex. While the topological structure is preserved, the geometric features are overlooked. [Miklos et al.(2010)] scales the medial ball and filters out the corresponding medial axis vertex when its ball is devoured by others. [Li et al.(2015), Pan et al.(2019)] propose a novel importance measurement, collapsing the medial axis edge with the lowest importance and generating a new medial axis point following the minimal quadratic error.

Another class of methods not only deletes the redundant branches of Voronoi subsets; instead, they obtain medial axis points first and leverage the properties of the (weighted) Voronoi diagram to establish the connectivity between these medial axis points. [Amenta et al.(2001)] takes a subset of Voronoi diagram vertices as “poles” and uses the weighted Voronoi diagram to obtain the topological connection between them. This structure is referred to as power shape. As the sampling density increases, this structure converges to the medial axis. To get a compact medial axis, [Dou et al.(2022), Wang et al.(2024a)] gradually select skeletal points from a set of candidate points until it reaches the number specified by the user, and infer connectivity from prim-

itive medial axis surface. [Wang et al.(2022)] propose a novel method to preserve the feature, especially for CAD-like models. Using a restricted power diagram, they optimize the position of the inner medial balls and connect them to create a medial mesh. [Wang et al.(2024b)] further enhances topological correctness while ensuring geometric features; however, the extensive use of tet slicing operations increases the computational overhead.

## 2.2 Learning-based Approaches

Currently, most learning-based methods rely on discrete approaches to construct the medial axis by identifying medial points and determining their connectivity. For instance, [Yang et al.(2020)] proposed a method to compute medial points with radius information from sparse point clouds by applying point-wise displacement vectors. They further introduced a rough tetrahedral simplification strategy to establish connectivity relationships for constructing the medial mesh. [Lin et al.(2021), Ge et al.(2023)] both focused on learning medial points with associated radius information. They employed Graph Auto-Encoder networks to establish connectivity relationships between these medial points to construct skeletal meshes. However, these approaches often encounter challenges such as insufficient reconstruction accuracy and incorrect topological connections. [Clémot and Digne(2023)] took a different approach by addressing the problem from a field perspective firstly, incorporating a total variation (TV) regularization term to improve the quality of the signed distance field (SDF). Then they traced medial points from surface points and used Mixed-Integer Linear Programming (MILP) to compute a simplified medial axis. Experimental results showed that this method handles noisy and incomplete point clouds effectively.

[Rebain et al.(2021)] explored the use of a differentiable continuous field to represent the medial axis, called the Medial Field (MF), and employed joint training to improve the accuracy of both the MF and the Signed Distance Field (SDF). However, while the approach demonstrated significant benefits in accelerating ray-surface intersection calculations, the authors did not fully explore its potential for medial mesh computation.

## 3 Preliminaries

Given a solid 3D shape  $\Omega$  with curved surface  $\partial\Omega$ , embedded in Euclidean space  $\mathbb{R}^3$ , the collection of all interior points is noted as  $\Omega^-$  and the exterior ones are  $\Omega^+$ . In this setting, this section will begin with a brief introduction to the popular terminology related to medial axis, SDF and UDF defined on  $\Omega$ , and further extend them to implicit medial axis representation.

### 3.1 Medial Axis

If  $p \in \mathbb{R}^3$  has more than one closest point to  $\partial\Omega$ ,  $p$  is a **medial point**, and the distance between  $p$  and one closest point is called the **radius**. **Medial axis (MA)**  $\mathcal{M}$  is defined as the collection of all medial points, which can also be regarded as the trajectory of the center of the maximum inscribed sphere. The part of medial axis located outside the shape is called the outer medial axis. Relatively, the inner part is called the inner medial axis. Medial axis associated with the radius of the maximally inscribed sphere is called **medial axis transform (MAT)**. In this paper, we focus on computing the inner medial axis transform, which we will refer to simply as “medial axis”  $\mathcal{M}_\Omega$  of  $\Omega$ . From the perspective

of the continuous distance field, medial points are local minima of the signed distance function of the shape. If we project an arbitrary point  $p \in \Omega^-$  to medial axis against the normal direction of its closest surface point, the **projected medial point** is noted as  $\mathcal{M}_{\text{proj}}(p)$ . It is akin to the outer point, with the distinction that the direction of movement must align with the normal vector.

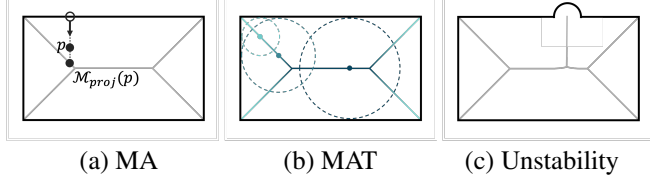


Figure 2: 2D illustration of the medial axis and medial axis transform. The medial axis, an unstable lower-dimensional representation of the original shape, is highly sensitive to boundary perturbations, which can significantly alter its topology.

$\mathcal{M}$  can be considered a lower-dimensional representation of  $\Omega$  because its geometric structure is a non-manifold curved surface rather than a solid shape with non-zero volume. It can precisely reconstruct the original shape by sweeping the space with spheres of varying radii. While the medial axis is inherently unstable; perturbations to the boundary can generate new branches and significantly increase its complexity, as Fig. 2 (c) shows.

### 3.2 Implicit Shape Representation

The distance field is an efficient yet powerful way to implicitly represent the shape. In this part, we will recall two popular distance field representations, **signed distance field (SDF)** and **unsigned distance field (UDF)**.

**SDF** The minimum distance between an arbitrary point  $p \in \mathbb{R}^3$  and  $\partial\Omega$  can be described by

$$d(p, \partial\Omega) = \inf_{q \in \partial\Omega} d(p, q),$$

where  $d(p, q)$  indicates the Euclidean distance between  $p$  and  $q$  and  $\inf$  means infimum. Then, SDF can be defined as

$$f_{\text{sdf}}(p) = \begin{cases} -d(p, \partial\Omega), & p \in \Omega^- \\ d(p, \partial\Omega), & p \in \Omega^+ \end{cases}$$

This is essentially a  $C^0$  continuity function and  $\partial\Omega$  is the zero level set. When  $\partial\Omega$  is piecewise smooth, its gradient satisfies the eikonal equation,  $|\nabla f_{\text{sdf}}(x)| = 1$ , only except for the points on the medial axis because it is not differentiable here. The direction is pointing outside and the gradient of surface points is exactly equivalent to the surface normal,

$$\nabla f_{\text{sdf}}(p) = N(p), \quad p \in \partial\Omega.$$

Fig. 3 (b) is a 2D illustration of the SDF.

**UDF** Similar to SDF, UDF also describes a distance field with the Euclidean distance metric. The difference is it does not report the signed information thus the value is positive for both interior and exterior as Fig. 3 (c) shows. Besides, it is not differentiable on the curved surface, which is the local minimal and the value is still zero. Owing to the omitting of the sign, UDF is capable of representing open surfaces and non-manifold structures.

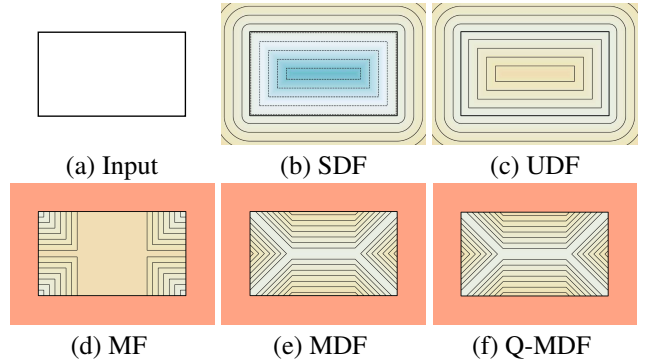


Figure 3: Distance fields and medial fields. Given a rectangle in (a), we visualize the signed distance field in (b), the unsigned distance field in (c), and the medial field in (d), respectively. In (e), we show the medial distance field, which is defined as the UDF of the medial axis. In (f), we show the quasi-medial distance field, computed by subtracting the SDF from the MF, effectively approximates MDF.

### 3.3 Implicit Medial Axis Representation

**Medial field** Introduced by [Rebain et al.(2021)], **medial field (MF)** is taken as the measurement of local thickness. For each point  $p$  in MF,  $f_{\text{mf}}(p)$  stores a scalar value representing the radius of  $\mathcal{M}_{\text{proj}}(p)$ , therefore,

$$f_{\text{mf}}(p) = f_{\text{sdf}}(\mathcal{M}_{\text{proj}}(p)). \quad (1)$$

This means that for any arbitrary point  $q \in \mathcal{M}$ , all points lying on the segment between  $q$  and its closest point on the surface share the same value. Thus for an arbitrary point  $p$ , its MF value cannot be lower than the absolute value of SDF:

$$f_{\text{mf}}(p) \geq f_{\text{sdf}}(p). \quad (2)$$

Fig. 3 (d) is an illustration of MF. Besides, [Rebain et al.(2021)] reveals the strong connection between SDF and MF: the gradient of MF is perpendicular to that of SDF, which means

$$\nabla f_{\text{sdf}}(p) \cdot \nabla f_{\text{mf}}(p) = 0. \quad (3)$$

Eq.1, Eq.2, and Eq.3 provide the necessary and sufficient conditions for a field to qualify as a medial field. A detailed proof can be found in [Rebain et al.(2021)].

**Deep medial field** According to above three conditions [Rebain et al.(2021)] define the medial axis in a variational way and offers three constraints for the **deep medial field (DMF)** training:

$$\mathcal{L}_{\text{max}} = \int_{\mathbb{R}^3} \max(f_{\text{sdf}}(x) - f_{\text{mf}}(x), 0)^2 dx \quad (4)$$

$$\mathcal{L}_{\text{ortho}} = \int_{\mathbb{R}^3} (\nabla f_{\text{sdf}}(x) \cdot \nabla f_{\text{mf}}(x))^2 dx \quad (5)$$

$$\mathcal{L}_{\text{consis}} = \int_{\mathbb{R}^3} (f_{\text{sdf}}(\mathcal{M}_{\text{proj}}(x)) - f_{\text{mf}}(x))^2 dx \quad (6)$$

The overall loss of MF training is given by

$$\mathcal{L}_{\text{MF}} = \lambda_{\text{max}} \mathcal{L}_{\text{max}} + \lambda_{\text{ortho}} \mathcal{L}_{\text{ortho}} + \lambda_{\text{consis}} \mathcal{L}_{\text{consis}} \quad (7)$$

It is worth noting that, although MF or DMF stores radius information about the medial axis, it is hard to capture the medial axis geometric structure directly from this field.

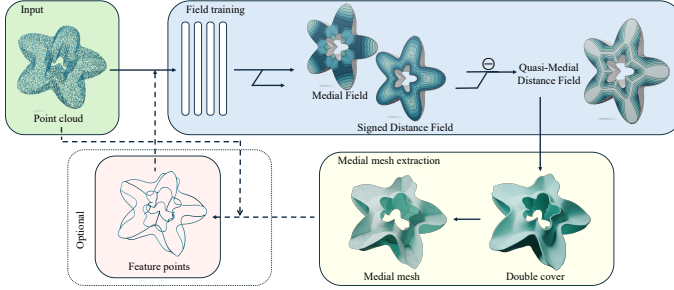


Figure 4: Pipeline of our medial axis computation method: The input consists of a point cloud or sampled points from a given mesh. After joint training of SDF and MF, we compute the implicit medial axis representation, called Q-MDF, by taking their difference. Then extract a double cover envelope of the medial axis, which is collapsed to form a zero-volume medial membrane afterward. In addition, it is optional to enhance the sharp feature by extracting feature points computed from input point cloud and medial membrane, and go through this pipeline again with this sharp feature constraint.

## 4 Method

Our learning-based method consists of two steps: (1) training to get the implicit representation of medial axis (Section. 4.1.3), and (2) extracting medial axis from this field (Section. 4.2). Additionally, a feature promotion strategy is proposed (Section. 4.3) for the shapes with sharp features, especially CAD models. Fig. 4 is the illustration of our pipeline.

### 4.1 Deep Medial Representation

#### 4.1.1 MDF

Because the medial axis  $\mathcal{M}$  of solid shape  $\Omega$  is a non-manifold curved surface, it is non-trivial to construct a differential field that can perfectly encode it. SDF and MF obliquely store the information of medial axis, but people cannot directly extract the iso-surface that represents medial axis from either SDF or MF. Considering the property of medial axis, UDF of medial axis is an ideal representation despite it is hard to compute. To separate the implicit representation of a solid shape and its medial axis, we call the UDF of the medial axis as **medial distance field (MDF)**. The formal definition of MDF is:

**Definition 1.** *Given a solid shape  $\Omega$ , suppose its medial axis is  $\mathcal{M}$ . For any point  $p \in \mathbb{R}^3$ , the closest point on  $\mathcal{M}$  is  $q$ . MDF value of  $p$  is defined as  $f_m(p) = \|p - q\|$ .*

Fig. 3 (e) is an illustration of MDF derived from the solid shape (Fig. 3 (a)). The MDF defined on  $\Omega^-$  is continuous with  $C^0$  smoothness, and the same applies to  $\Omega^+$ . But there may be a discontinuity at the boundary. To better understand the characteristics of MDF, we will focus on  $\Omega^-$  and discuss it in the following sections. It is easy to see that  $p \in \mathcal{M}$ ,  $f_m(p) = 0$ .  $f_m(p)$  goes higher as  $p$  leaves  $\mathcal{M}$ . If we select a small  $\epsilon$  value and look at the  $\epsilon$ -level set, it will resemble a membrane outlining the medial axis, which is homotopy equivalent to both the medial axis and the overall shape [Biasotti et al.(2008)].

It is worth noting that computing an accurate medial axis is notoriously challenging, especially for shapes with complex topology and bumpy surfaces. Therefore, directly computing the MDF for a solid shape is generally difficult.

#### 4.1.2 Q-MDF

Due to the challenges in obtaining the MDF, we proposed an alternative implicit representation that is similar to MDF and more easily to compute, which is called **quasi-MDF (Q-MDF)**. This structure is derived from the observation that the absolute SDF value climbs against the gradient direction and reaches its maximum at  $p \in \mathcal{M}$ , where  $f_{mf}(p) = |f_{sdf}(p)|$  holds. Therefore, by subtraction of these two fields, we can get a continuous new field Q-MDF. Its definition is:

**Definition 2.** *For a solid shape  $\Omega$ , suppose its SDF  $f_{sdf}$  and MF  $f_{mf}$  are given. For any point  $p \in \mathbb{R}^3$ , Q-MDF value of  $p$  is defined as  $f_q(p) = f_{mf}(p) - |f_{sdf}(p)|$ .*

Q-MDF is similar to MDF according to its definition; the value at  $\mathcal{M}$  is zero and goes up when leaving from the medial axis. Fig. 3 (f) is a 2D illustration of Q-MDF. When extracting level sets from Q-MDF and MDF using the same  $\epsilon$  value, the membrane area of Q-MDF is slightly larger than that of MDF, although the overall shapes are similar. Therefore, Q-MDF can serve as an ideal substitute for MDF and facilitate the training process, as MDF is difficult to formulate.

#### 4.1.3 Joint Training for Q-MDF

In our training, the basic structure is as in [Chen and Zhang(2019), Park et al.(2019)], a multi-layer perceptron (MLP) network operating on the coordinates of an input point. Following [Rebain et al.(2021)], we employ a multi-headed neural network structure to predict both the SDF and the medial field (inside and outside fields,  $M^-(x)$  and  $M^+(x)$ ), with the final output selected based on the sign of the SDF through separate MLP heads. After obtaining a well-trained MF and SDF, we compute the Q-MDF by taking their difference.

## 4.2 Extracting Medial Mesh from Q-MDF

Extracting medial mesh from Q-MDF consists of a two-stage operation: (1) extracting a watertight thin sheet manifold containing the entire medial axis, and (2) shrinking this shape to 0 volume to approximate the medial axis. The final medial axis transform is constructed from this medial membrane, with the associated radius information for each vertex retrieved from the SDF.

**$\epsilon$  covering extraction** Inspired by [Hou et al.(2023)], the initial mesh is computed using the conventional marching cubes method [Lorensen and Cline(1998)] to extract the  $\epsilon$ -iso surface of the Q-MDF, resulting in a watertight representation that covers the entire medial axis. It is worth noting that, for a standard Q-MDF, the value is exactly 0 at the medial axis. When  $\epsilon$  is small enough, the reconstructed  $\epsilon$  coverage is homotopy equivalent to the medial axis, so as to the original shape. However, for the deep Q-MDF obtained from joint training, the value at the medial axis is not always zero, thus the value of  $\epsilon$  should not be too small. In practice,  $\epsilon$  is also relevant to marching cube depth. In our implementation, when the depth is 8, setting  $\epsilon$  to 0.005 is suitable for most circumstances.

**Shrink to medial axis** After obtaining the  $\epsilon$  iso-surface of Q-MDF, this volumetric thin sheet should shrink to zero volume to approximate the real medial axis, a non-manifold curved surface.

This mapping  $\pi$  is obtained through the following optimization:

$$\min_{\pi} \lambda_1 \text{Vol}(\mathcal{S}_\epsilon) + \lambda_2 \sum_{v \in \mathcal{S}_\epsilon} w(v) \left\| \pi(v) - \frac{1}{\mathcal{N}(v)} \sum_{v_i \in \mathcal{N}(v)} \pi(v_i) \right\|^2,$$

where  $\mathcal{S}_\epsilon$  indicates the  $\epsilon$  iso-surface and  $\text{Vol}(\mathcal{S}_\epsilon)$  is the volume of it. The second term is a surface Laplacian constraint. The weight  $w(v)$  of a vertex  $v$  is inversely correlated with the total area of the adjacent triangles, as defined in [Hou et al.(2023)]. Here,  $\mathcal{N}(v)$  denotes the one-ring neighboring vertices of  $v$ .

### 4.3 Sharp Feature Consolidation

When the shape has sharp features, the mathematically defined medial axis should extend to the feature lines, with the radius at the feature lines being zero [Wang et al.(2022)]. However, the Q-MDF obtained from joint training tends to be smooth if no feature priors are incorporated, causing the resulting medial axis to not extend precisely to the feature lines. This sharp feature consolidation strategy provides a detachable module to promote both the quality of the medial axis and field representation on sharp features. In Section 4.3.1, we will explore how to infer sharp feature points from the input point cloud using the existing medial mesh. In Section 4.3.2, we will discuss how incorporating feature point priors can enhance the joint training of SDF and MDF.

#### 4.3.1 Medial Axis Guided Feature Detection

**Sharp feature and medial axis boundary** It is well-known that the medial axis is a non-manifold curved surface, and its boundary is defined as a collection of points whose neighborhood is homomorphic to a half-disk. In a discrete mesh setting, this can be easily identified by collecting all the edges that are adjacent to only one face. However, the medial mesh extracted by our method is essentially a watertight manifold, which prevents us from directly extracting the boundary by simply checking the number of adjacent faces. Due to the zero-volume nature of our medial mesh, sharp turns occur at the boundary. Thus, we can identify the boundary by checking the dihedral angle. If the dihedral angle of an edge is close to  $2\pi$ , that edge is considered a boundary edge.

For shapes with sharp features, the medial axis extends to these features, meaning the boundary of the medial axis coincides with the sharp features of the shape. When the learned MF and SDF are often overly smoothed at sharp features, the extracted medial axis may not fully extend to the feature lines. However, the boundary of the medial axis still points towards the sharp features. Therefore, if the boundary of the medial axis exhibits both low MF and SDF values, it should be extended toward the latent sharp feature.

**Prominent feature points generation** After identifying the medial axis boundary that points to latent sharp features, we uniformly sample a set of points on it and use a marching-like method to infer the feature points. Fig. 5 provides a 2D illustration of feature point inference. First of all, for a given boundary point  $p$  where marching is needed, let its two bilateral SDF gradients be  $g_1(p)$  and  $g_2(p)$ . The marching direction is determined by  $g_1(p) + g_2(p)$ . Next, we march along this direction according to the distance to the closest surface point, continuing until the distance starts to increase. The currently inferred feature point may not be precisely accurate and

could be inconsistent with neighboring feature points. Therefore, we identify the  $k$  nearest surface points to this initially inferred point and adjust its position using the quadric error metric (QEM). For more details on the computation of QEM, please refer to [Garland and Heckbert(1997)].

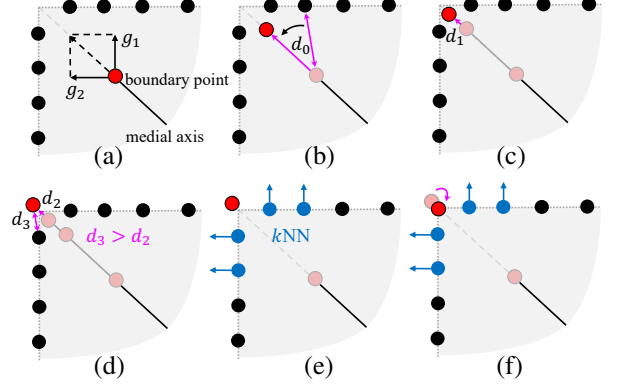


Figure 5: Locating feature points. (a) The marching direction is determined by the sum of the bilateral gradients at the boundary point. (b)-(d) The boundary point is shifted along the marching direction by the closest distance  $d_i$  until the closest distance begins to increase. (e) Identify the  $k$  nearest surface points to the shifted boundary point. (f) Employ a quadratic error metric to determine the feature point for this corner.

#### 4.3.2 Training with Feature Prior

Prominent feature point set  $P$ , whether inferred from a point cloud or computed from the input mesh using a user-defined dihedral angle threshold, can be utilized to enhance the joint training of SDF and MF through additional loss terms:

$$\mathcal{L}_{\text{sharp1}} = \sum_{i=1}^n f_{\text{sdf}}(p_i),$$

and

$$\mathcal{L}_{\text{sharp2}} = \sum_{i=1}^n f_{\text{mf}}(p_i).$$

$\mathcal{L}_{\text{sharp1}}$  and  $\mathcal{L}_{\text{sharp2}}$  are used to force the value at feature points to be zero.

## 5 Evaluation and Comparison

### 5.1 Experimental Setting

**Implementation Details** All tested shapes are regularized into a unit box, centered at the origin. For point cloud inputs, the points are directly fed into the network. For mesh inputs, we densely sample points on the surface and feed them into the training network. Both input types are processed in batches of 4096 points, and neither requires additional normal information. The SDF and MF joint network training follows the architecture proposed in [Rebain et al.(2021)]. The detailed parameter setting of extracting the double cover from Q-MDF will be discussed later. All experiments were conducted using an NVIDIA 4090 graphics card with 24 GiB of video memory.

**Evaluation Metrics** Following the conventional criteria for medial axis, we use reconstruction accuracy to evaluate the reconstruction ability of the medial axis transform. In mathematics, the reconstructed shape is defined as the swept space of a

varying radius sphere. As described in [Li et al.(2015)], the reconstructed shape is computed as a union of a set of enveloping volumes of its medial primitives. Then, reconstruction accuracy can be quantified using two metrics: the two-sided mean distance error, measured by **Chamfer distance (CD)**, and the two-sided maximum distance error, measured by **Hausdorff distance (HD)**.

We use the **Euler characteristic (EC)**, defined as  $\mathcal{X} = V - E + F$  to evaluate the topological correctness of medial axis. Notably, our method produces a medial membrane, a 2D manifold watertight mesh, which should have the same EC as the original shape. In contrast, the medial mesh, being a 2D non-manifold curved surface, may have an EC that differs from that of the original shape.

We apply **boundary smoothness** to evaluate the compactness of medial axis. Boundary smoothness is measured by average curvature  $C_{\text{avg}}$ , which is formulated as:

$$C_{\text{avg}} = \frac{1}{\mathcal{L}} \int_0^{\mathcal{L}} \kappa(s) ds,$$

where  $\kappa(s)$  indicates curvature, and  $\mathcal{L}$  is the total length of curve. For a discrete curve composed by a string of points  $C$ ,  $C_{\text{avg}}$  can be formulated as:

$$C_{\text{avg}} = \frac{1}{\mathcal{L}} \sum_{i=1}^n l_i \theta_i,$$

where  $l_i = \frac{\|c_{i-1} - c_i\| + \|c_{i+1} - c_i\|}{2}$ ,  $\theta_i = \pi - \arccos\left(\frac{(c_{i-1} - c_i) \cdot (c_{i+1} - c_i)}{\|c_{i-1} - c_i\| \cdot \|c_{i+1} - c_i\|}\right)$  and  $n$  is the number of turning angles  $\theta$ .

## 5.2 Deep Q-MDF Based Medial Axis

### 5.2.1 Deep Q-MDF

The learned deep Q-MDF from joint training closely resembles the ground truth Q-MDF. Since the training loss terms are applied across the entire space, the resulting field satisfies variational requirements not only near the surface but also far from it. Therefore, the resulting Q-MDF values around the medial axis are reliable, allowing a small threshold,  $\epsilon$ , to be used for extracting the initial double-cover that tightly wraps the medial axis. Fig. 6 illustrates a comparison between our resulting field and the ground truth, along with the extracted  $\epsilon$  level set. In this case, the marching cubes resolution is  $256^3$  and  $\epsilon = 0.005$ . The Euler characteristic of the extracted  $\epsilon$  iso-surface is 0, which is the same as the input solid shape.

### 5.2.2 Shrinking with diverse $\epsilon$

The zero-volume constraint is effective across a wide range of  $\epsilon$  values. As Fig. 7 depicts, as the  $\epsilon$  value increases, the volume of the initially extracted double cover also grows. However, after 3K iterations of shrink optimization, all three cases ultimately converge to a near-zero volume. Additionally, when  $\epsilon$  is small, the double-cover structure aligns closely with the original medial axis, resulting in more precise optimization during the contraction process. If  $\epsilon$  is too large, and the shell cavity becomes too thick, redundant branches may be produced after shrink optimization.

### 5.2.3 Localized symmetric pattern

An interesting characteristic of MF-involved training is that the resulting neural shape representation tends to recover the latent

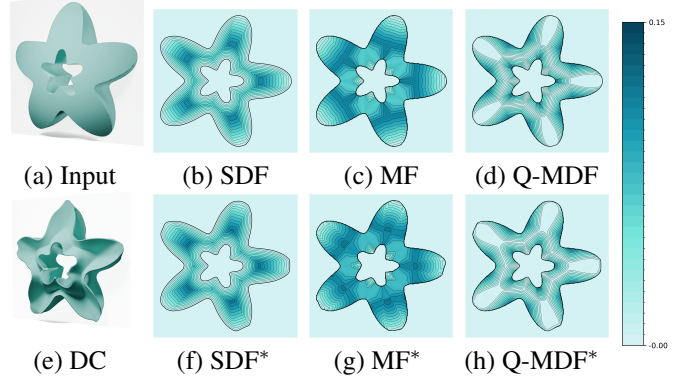


Figure 6: Analysis of the learned fields: (a) Input shape with a cut plane; (b)-(d) are our differential fields on the cut plane. (f)-(h) are corresponding ground truth. (e) initial double cover extracted from our Q-MDF with  $\epsilon = 0.005$ .

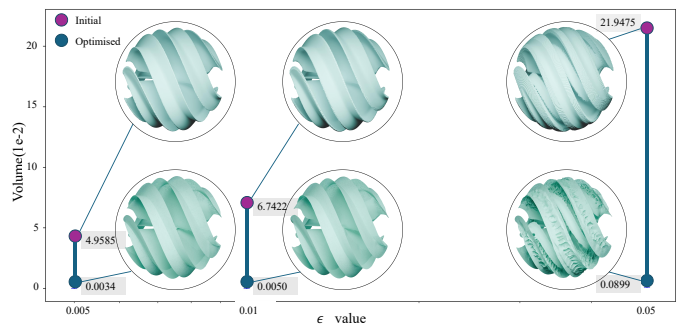


Figure 7: This figure shows the shrinking results with different  $\epsilon$  values, illustrating the initial  $\epsilon$  double cover for  $\epsilon = 0.05, 0.01$ , and  $0.005$ , respectively, and their shrink optimization results after 3K iterations.

shape with localized symmetry, leading to a surface with higher-order smoothness. As Fig. 8 shows, the input is a Dupin cyclide point cloud, partially cut artificially. For pure SDF learning without MF constraints, after 500k iterations, the shapes tend to directly fill the gaps, as shown in Fig. 8 (b). However, with localized symmetric guidance from the MF constraints, the inferred shape ‘inflates’ in the missing regions, closely approximating the original shape, as seen in Fig. 8 (c). In this case, the extracted medial axis is smooth and concise, as shown in Fig. 8 (d).

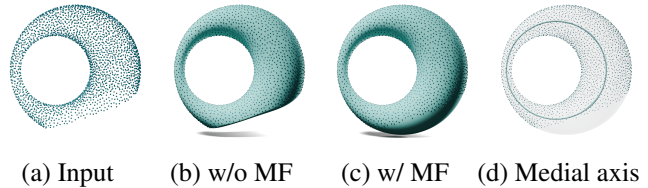


Figure 8: Utilize a partially missing Dupin cyclide point cloud as input and train the model with or without the MF constraints. (b) and (c) are extracted zero iso-surface from the corresponding SDF. (d) demonstrates the medial axis computed from the fields with MF constraint. It is evident that MF-related constraints promote a better inferring of the latent shape with higher smoothness and result in a concise medial axis.



Figure 9: Gallery of our results, showcasing a range of challenging and classical models, along with models from commonly used datasets (Thingi10k [Zhou and Jacobson(2016)], ABC [Koch et al.(2019)], SRB [Huang et al.(2024)]).

#### 5.2.4 Sharp feature consolidation

Sharp feature consolidation is an optional procedure that can be applied to improve accuracy around sharp features in some CAD models. When needed, we can add this module to refine the field near sharp features. To evaluate its effectiveness, we use a point cloud as input, compute a coarse medial axis, and identify prominent feature points. These points are then used as additional constraints to train the fields and recompute the medial axis. The resulting Q-MDF computed with feature constraints is significantly more accurate around sharp features; the values at the medial axis are closer to zero compared to the Q-MDF learned without feature constraints. This sharp feature enhancement notably improves the extracted medial axis and can even extend to feature lines, as demonstrated in Fig. 10.

Datasets	CD ( $10^{-3}$ )	HD ( $10^{-3}$ )
ABC [Koch et al.(2019)]	1.6004	20.3596
Thingi10K [Zhou and Jacobson(2016)]	2.6029	18.9215
SRB [Huang et al.(2024)]	2.1010	15.8574

Table 1: For three datasets with diverse inputs, this table collects the average Chamfer distance (CD,  $10^{-3}$ ) and Hausdorff distance (HD,  $10^{-3}$ ) of surfaces reconstructed from our resulting medial axes.

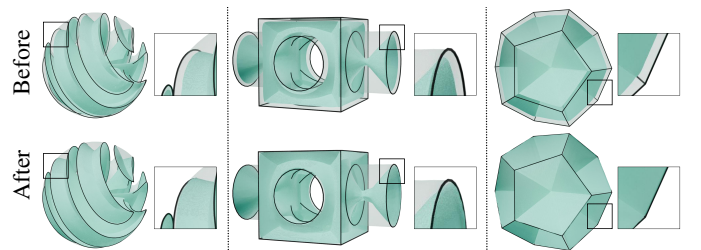


Figure 10: Sharp feature enhancement effectively draws the medial mesh, originally distant from sharp features, closer to them. This adjustment significantly improves the quality of the extracted medial meshes.

#### 5.2.5 Exhaustive experiments

Our method is robust and has low requirements for the input shape: it does not need a watertight manifold mesh or a densely sampled surface. The input can be a mesh with open boundaries, a triangle soup, or a sparse point cloud. In this section, we present comprehensive experiments conducted on three types of datasets: ABC [Koch et al.(2019)], Thingi10k [Zhou and Jacobson(2016)], and Surface Reconstruction Benchmark (SRB) [Huang et al.(2024)]. The ABC dataset consists of numerous CAD meshes, while Thingi10K provides more complex geometric models with defects such as open

	Input				Output	Homotopy	Compactness
	watertight mesh	mesh with defects	dense point cloud	sparse point cloud			
PC [Amenta et al.(2001)]	-	-	✓	✗	Medial mesh	Conditional	✗
SAT [Miklos et al.(2010)]	✓	-	✓	✗	Medial mesh	Conditional	✗
Q-MAT [Li et al.(2015)]	✓	-	✗	✗	Skeletal mesh	Conditional	✓
VC [Yan et al.(2018)]	✓	✗	✗	✗	Medial mesh	Conditional	✗
CoverageAxis++ [Wang et al.(2024a)]	✓	-	✓	✗	Skeletal mesh	No	✓
MATPF [Wang et al.(2022)]	✓	✗	✗	✗	Medial mesh	No	✓
MATTOP [Wang et al.(2024b)]	✓	✗	✗	✗	Medial mesh	Yes	✓
DPC [Wu et al.(2015)]	-	-	✓	✓	Meso-skeleton	-	-
Point2Skeleton [Lin et al.(2021)]	-	-	✓	✓	Skeletal mesh	No	✓
NeuralSkeleton [Clémot and Digne(2023)]	-	-	✓	✓	Skeletal mesh	No	✓
Ours	✓	✓	✓	✓	Medial membrane	Conditional	✓

Table 2: Summary of 10 selected 3D medial axis approximation methods.

	bunny			kitten			holes			cheeze			trim-star			block			sharp-sphere		
	CD	HD	EC	CD	HD	EC	CD	HD	EC	CD	HD	EC	CD	HD	EC	CD	HD	EC	CD	HD	EC
PC	0.54	25.76	76422	0.83	15.22	78025	0.38	7.97	35962	4.56	48.8	85459	0.81	17.48	30901	1.67	32.84	33418	1.16	40.01	62960
CoverageAxis++	10.26	64.64	37	24.64	88.02	14	36.02	88.71	7	28.17	81.5	-11	26.46	85.93	147	27.71	100.38	32	30.38	115.12	28
Q-MAT	5.12	127.83	3	3.37	15.75	2	2.46	9.36	-2	2.05	16.84	93	4.58	34.14	1	5.78	62.16	9	5.75	67.37	4
VC	16.37	104.48	1	2.77	12.55	264	2.21	9.39	-2	-	-	10004	4.09	26.71	3	4.84	25.22	33	7.06	72.14	77
SAT	12.46	50.8	47	12.93	32.18	85	7.34	14.19	55	3.37	12.47	40	5.88	14.26	72	6.56	18.95	119	9.08	45.89	63
MATPF	1.94	39.98	8	0.79	24.43	5	0.49	8.12	-2	0.28	10.22	-19	0.99	15.88	0	0.32	9.63	-2	0.68	16.47	1
MATTOP	2.01	16.93	1	1.61	25.91	0	0.8	8.75	-2	1.18	10.71	-19	0.78	8.71	0	0.97	24.1	-2	1.7	23.39	1
NeuralSkeleton	-	-	77	-	-	44	-	-	39	-	-	147	-	-	177	-	-	213	-	-	190
Ours	1.86	12.56	2	1.58	19.96	0	0.89	9.74	-4	3.12	32.58	-38	0.86	16.54	0	0.95	21.41	-4	1.67	19.69	2

Table 3: Statistical data comparing the reconstructed surface accuracy and topological correctness of the medial mesh for eight methods and ours. Chamfer distance (CD) and Hausdorff distance (HD) are scaled by  $10^3$ . The Euler characteristic reflects the topology of the medial axis. Both MATTOP and our method produce medial axes with correct topology.

Figure 11: Medial axes of the bunny model, computed by SAT [Miklos et al.(2010)], VC [Yan et al.(2018)], MATPF [Wang et al.(2022)], MATTOP [Wang et al.(2024b)] and our method. The boundaries are visualized in black. Our method produces a visually more compact and smooth result, whereas others tend to suffer from excessive branching or jagged boundaries.

boundaries, self-intersection and non-manifold. The Surface Reconstruction Benchmark (SRB) covers a variety of point cloud inputs. For each dataset, we selected the first 30-50 models to carry out the experiments. The statistical data can be found in Table 1. Additionally, we experimented with some challenging point cloud inputs and commonly used geometric models, as shown in Fig. 9.

### 5.3 Comparison

In this section, we compare our method with 10 representative approaches. In addition to evaluating geometric and topological correctness, we also assess each method's ability to handle challenges such as thin sheets, sparse point clouds, and noisy data. A quantitative summary of the results is provided in Table 2.

#### 5.3.1 Geometry and topology accuracy

In this section, we evaluate the reconstruction ability and topological accuracy of the generated medial axis on simple solid shape input. The reconstruction ability is measured using Chamfer distance (CD) and Hausdorff distance (HD) between the reconstructed surface mesh and the ground truth. Topological accuracy is evaluated using the Euler characteristic (EC). It is important to note that the DPC method produces a meso-skeleton (a point set rather than a medial mesh) combined with consolidated surface points, and thus is excluded from the quantitative comparison for fairness. For all compared methods, we carefully adjusted the parameters to achieve reasonable medial axis. The statistical data in Table 3 shows that, for organic models (the first three columns), owing to the medial mesh computed from PC without pruning records more detailed information, the reconstructed surface is best approximated to the original shape. For CAD-like shapes (the last three columns), feature preserving methods, MATPF and MATTOP have the best performance. Although our method produces a relatively compact medial axis, it

still maintains stable and fairly good geometric accuracy across both types of models. In terms of geometric accuracy, the Euler characteristic data shows that both our method and MATTOPo maintain homotopy equivalence with the input shape, whereas other methods do not.

### 5.3.2 Smoothness

This smoothness comparison is only performed on methods capable of generating a “clean” medial mesh, defined as a 2D non-manifold curved surface without cavities. The boundaries of these medial meshes are extracted by identifying triangular faces with only one adjacent face. The boundary of our medial membrane is determined by the dihedral angle as discussed in Section 4.3. For CAD-like models, the medial meshes produced by MATFP and MATTOPo ideally extend to sharp features, allowing them to perform best, with smoothness determined by the shape’s sharp features. However, for organic models, our method produces more stable boundaries and shows a clear advantage over other approaches. A direct visual comparison for the organic model is provided in Fig. 11. For a detailed quantitative comparison, please refer to Table 4.

	SAT	VC	MATFP	MATTOPo	Ours
Bunny	0.40	0.73	1.02	0.98	0.07
Dodecahedron	0.48	0.84	1.18e-6	1.11e-2	1.55e-2

Table 4: Quantitative comparison of boundary smoothness for organic and CAD models, evaluated among our method, SAT [Miklos et al.(2010)], VC [Yan et al.(2018)], MATFP [Wang et al.(2022)], and MATTOPo [Wang et al.(2024b)].

### 5.3.3 Thin sheet

For models containing thin plates or tubes, most methods that rely on surface sampling or voxelization are delicate to parameter variations. As Fig.12 shows, the input dolphin model is thin at its fin and flipper. When resolution is not high enough, extracting the entire medial axis at these thin areas is hard for VC. It is also difficult to achieve sufficiently dense sampling, making it challenging for surface-sampling-based methods like SAT, PC and MATFP to produce topologically correct and geometrically accurate results. The meso-skeleton produced by DPC risks shifting away from the center, and fewer medial points are generated in regions where there is a significant jump in medial radius. MATTOPo, by gradually adding points and detecting topology correctness, can effectively and automatically explore thin plate regions. It generates a medial axis that is both geometrically and topologically accurate, with its results being relatively insensitive to the parameter. For default parameters, our method can generate reasonable Q-MDF at thin sheet areas. It is easy to extract a compact medial axis that is homotopy equivalent to the input shape.

### 5.3.4 Sparse input

For most traditional methods that support point clouds as input, surface sampling density is a critical factor that significantly affects the quality of the resulting medial axis, and even its correctness. Fig. 13 provides an example. The first two inputs are uniformly sampled sparse points on a teacup model, with the second being even sparser. The last input is a point cloud with varying density. For the representative classical computational

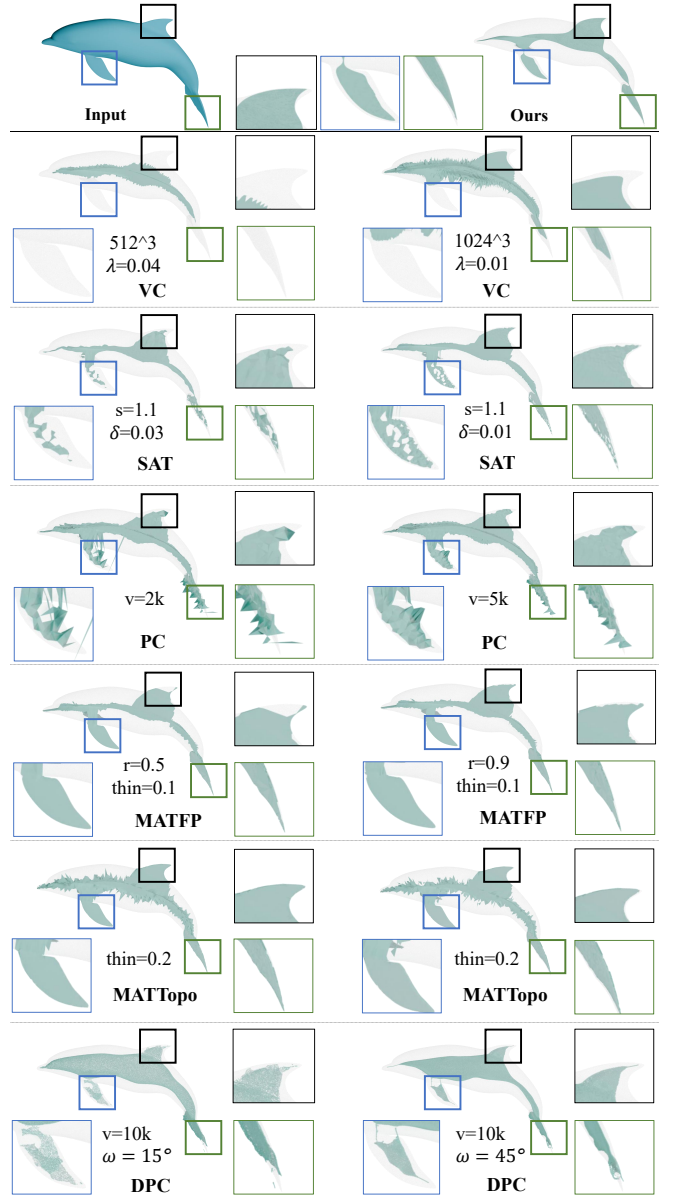


Figure 12: Qualitative comparison of our method with VC [Yan et al.(2018)], SAT [Miklos et al.(2010)], PC [Amenta et al.(2001)], MATFP [Wang et al.(2022)], MATTOPo [Wang et al.(2024b)] and DPC [Wu et al.(2015)] on the Dolphin model, which features multiple thin structures on its tail and fins. For each baseline method, results are shown with two different parameter settings, accompanied by close-up views to highlight the details. Our method effectively manages these thin structures, producing compact medial mesh superior both in geometry and topology.

geometry method, PC, as the input point cloud becomes sparser, both the centrality and smoothness of the medial axis degrade. In cases of extreme sparsity, identifying the inner poles becomes difficult. DPC outperforms PC when handling sparse point cloud inputs, but the connection part between the teacup handle and the cup body tends to suffer from geometric and topological inaccuracies. Similarly, when the point cloud is sparse, Point2Skeleton struggles to identify interior points and construct correct connections. NeuralSkeleton (NSK), aided by shape inference through learning, produces a more reasonable medial mesh, but holes

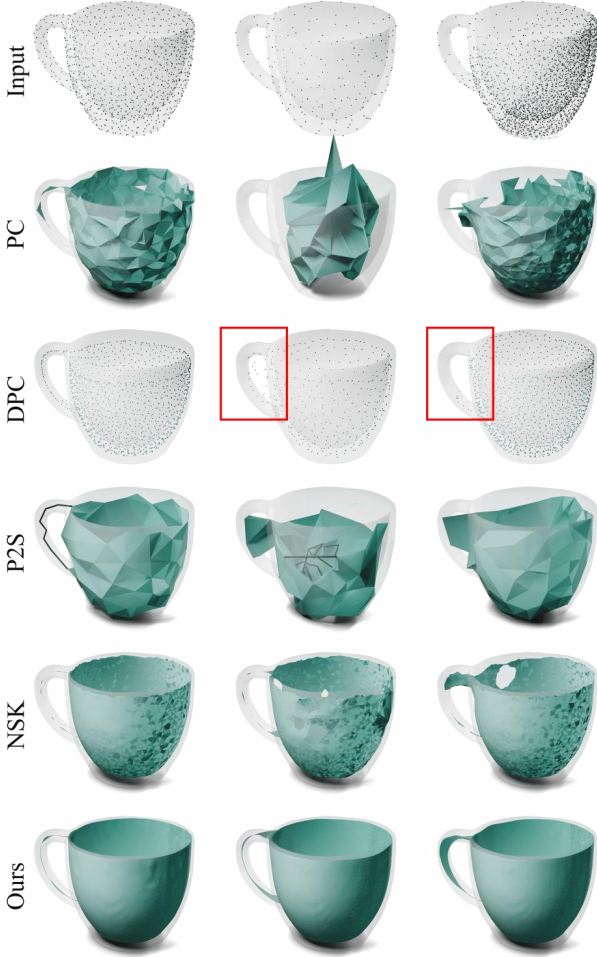


Figure 13: Comparison across varying point cloud density inputs. The first two columns show the results from uniform sampling with different densities, while the input for the last column has varying sampling density.

can appear when the input is extremely sparse. In contrast, our method shows more stable performance when dealing with diverse sparse inputs. In the three illustrated cases, the medial axis computed using our method consistently preserves the same topology as the original shape, while also maintaining good centering and smoothness.

In addition to handling uniformly sampled sparse inputs, our method is also capable of managing more extreme cases, such as wireframe inputs. Fig. 14 shows the extracted medial axis and the reconstructed surface for the wireframe model from [Huang et al.(2019)].

### 5.3.5 Incomplete input

When the input is a point cloud with missing patches, inferring a centralized medial axis becomes a challenging task for most traditional methods. For instance, Fig. 17 shows an input point cloud with partially missing patches. Using this as input for PC, the resulting medial axis bends toward the missing area or protrudes outside the latent surface. The associated radius is exceptionally high for the vertices in these areas, resulting in poor surface reconstruction from the medial axis transform in those regions. DPC infers a complete surface sampling using its localized symmetry properties, resulting in a centered point set

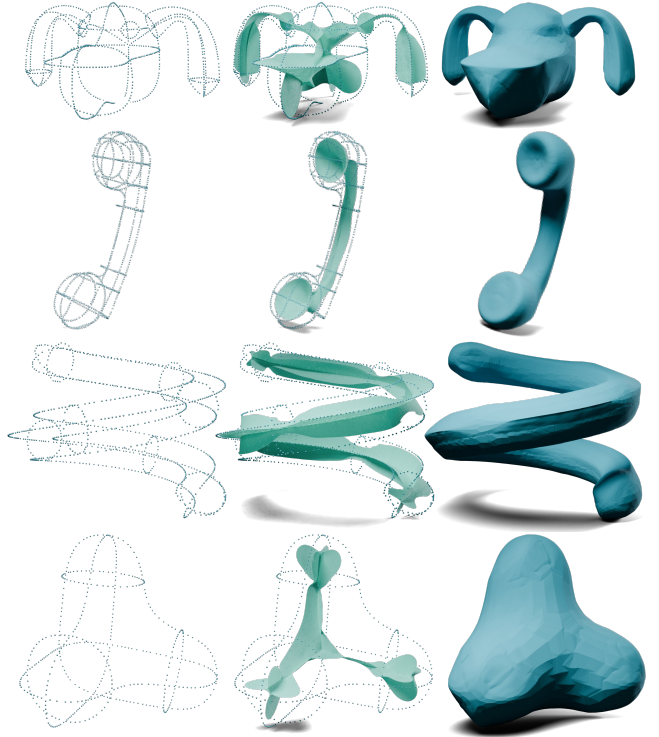


Figure 14: From left to right: the wireframe inputs [Huang et al.(2019)], our computed medial axis, and the reconstructed surfaces.

known as the meso-skeleton. It reconstructs the surface directly from the enhanced surface sampling by utilizing Poisson reconstruction [Kazhdan and Hoppe(2013)]. The overall result appears plausible, but when the missing data is significant, it tends to infer the shape with spherical artifacts. Thanks to the implicit representation of the shape with localized symmetry patterns, the medial structure computed by our method is centralized, and the reconstructed surface is visually consistent and tight.

### 5.3.6 Noise

In this subsection, we evaluate the impact of noise on computing the medial axis. The inputs consist of three sets of points sampled from the elephant surface with 0.1%, 0.25%, and 0.5% noise. As shown in Fig. 15, as the noise level increases, the resulting medial mesh from PC tends to protrude outside the surface, leading to topological errors such as extra holes or redundant connections. DPC takes in a noisy point cloud with correct normals, and while the overall shape appears reasonable, the meso-skeleton may shift off-center. Both NeuralSkeleton and our method are resistant to noise, consistently producing centered and compact medial axes. While for CAD-like models, NeuralSkeleton tends to be too simplified to encode the entire shape.

### 5.3.7 Real scan

We also evaluate the performance of our method on real scan data from the Surface Reconstruction Benchmark (SRB) [Berger et al.(2013)]. These point clouds present challenges such as noise, misalignment, and missing patches. As depicted in Fig. 16, the top row features a CAD model, Daratech, which has a large area of missing points where the camera couldn't capture the surface. Our method successfully handles this defect, producing a tight reconstruction. The next three rows depict organic

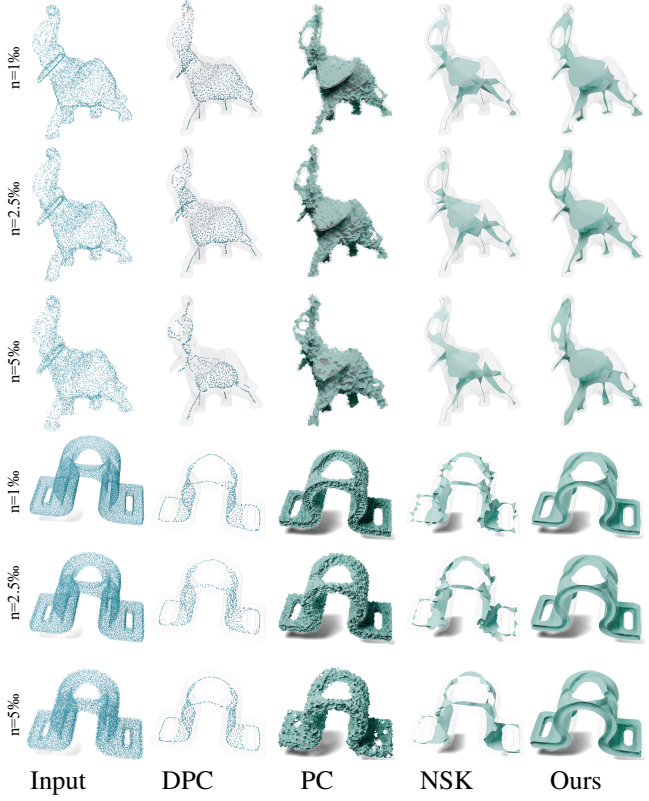


Figure 15: Comparison of medial axis computation under varying levels of noise. For each model, the noise level increases from top to bottom. Large amounts of noise have a significant impact on the PC [Amenta et al.(2001)] method, while DPC [Wu et al.(2015)], NeuralSkeleton (NSK) [Clémot and Digne(2023)], and our method show greater resistance to high noise levels to some extent.

models, where our method results in a compact medial axis with a visually reasonable topology and smooth reconstructed shapes.

## 6 Conclusion and Future Work

In this paper, we introduce a novel method for computing the medial axis transform. Unlike traditional computational geometry approaches, which have strict input requirements and can encounter numerical robustness issues, our method leverages a variational representation of the medial axis. This allows us to robustly extract a compact medial membrane mesh from a variety of input types.

However, there are still several issues that need to be addressed. First, the membrane mesh is a double-layer structure, with no direct correlation between the two overlapping patches, making it difficult to convert into a 2D non-manifold medial mesh. Second, we currently use an MLP network to jointly train MF and SDF, which is computationally expensive and limits the practicality of our method. Third, to further improve the topology, incorporating an additional check for local feature size (which is the MF value exactly) and using an adaptive marching cubes algorithm could be beneficial.



Figure 16: Our medial mesh and the corresponding reconstruction results on real-world scan data.

## References

- [Amenta et al.(2001)] Nina Amenta, Sunghee Choi, and Ravi Krishna Kolluri. 2001. The power crust, unions of balls, and the medial axis transform. *Computational Geometry* 19, 2-3 (2001), 127–153.
- [Attali and Montanvert(1996)] Dominique Attali and Annick Montanvert. 1996. Modeling noise for a better simplification of skeletons. In *Proceedings of 3rd IEEE International Conference on Image Processing*, Vol. 3. IEEE, 13–16.
- [Berger et al.(2013)] Matthew Berger, Joshua A Levine, Luis Gustavo Nonato, Gabriel Taubin, and Claudio T Silva. 2013. A benchmark for surface reconstruction. *ACM Transactions on Graphics (TOG)* 32, 2 (2013), 1–17.
- [Biasotti et al.(2008)] Silvia Biasotti, Dominique Attali, Jean-Daniel Boissonnat, Herbert Edelsbrunner, Gershon Elber, Michela Mortara, Gabriella Sanniti di Baja, Michela Spagnuolo, Mirela Tanase, and Remco Veltkamp. 2008. Skeletal structures. *Shape Analysis and structuring* (2008), 145–183.
- [Blum(1967)] Harry Blum. 1967. A Transformation for Extracting New Descriptors of Shape. In *Models for the Perception of Speech and Visual Form*, Weiant Wathen-Dunn (Ed.). MIT Press, Cambridge, 362–380.
- [Brandt(1994)] Jonathan W Brandt. 1994. Convergence and continuity criteria for discrete approximations of the continuous planar skeleton. *CVGIP: Image Understanding* 59, 1 (1994), 116–124.
- [Chazal and Lieutier(2005)] Frédéric Chazal and André Lieutier. 2005. The “ $\lambda$ -medial axis”. *Graphical models* 67, 4 (2005), 304–331.

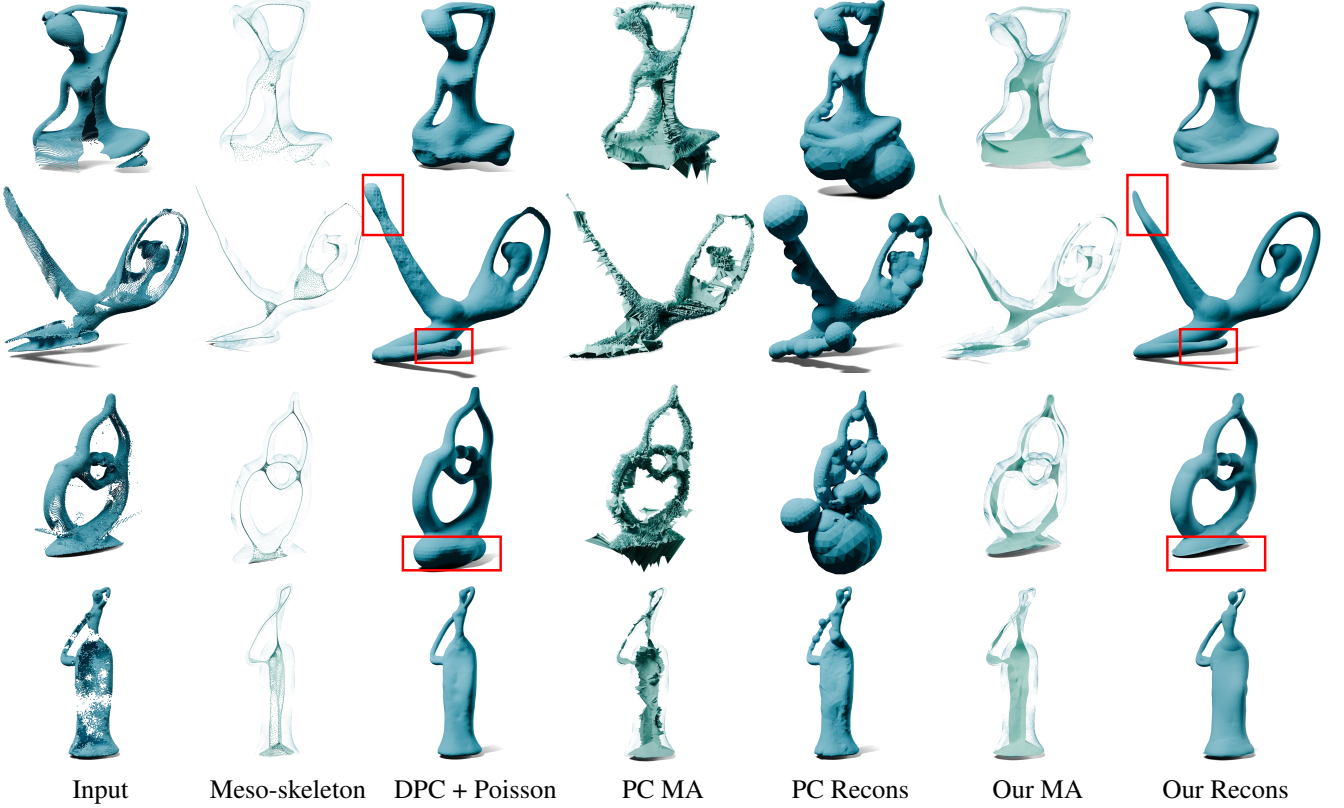


Figure 17: Comparison of our method with DPC [Wu et al.(2015)] and PC [Amenta et al.(2001)] on point clouds with partially missing data. From left to right: the input point clouds, the meso-skeletons and the corresponding Poisson reconstruction generated from DPC surface samplings, the medial meshes computed by PC, the surfaces reconstructed from PC medial meshes, the medial meshes produced by our method, and the surfaces reconstructed from our medial meshes. Despite the partially missing data, the input point clouds exhibit strong cyclide-like local geometry. Our method, aimed at simplifying the medial axis, successfully recovers the medial axis from these incomplete inputs, leading to reconstructed surfaces that effectively fill in the missing components.

[Chazal and Lieutier(2008)] Frédéric Chazal and André Lieutier. 2008. Smooth manifold reconstruction from noisy and non-uniform approximation with guarantees. *Computational Geometry* 40, 2 (2008), 156–170.

[Chen and Zhang(2019)] Zhiqin Chen and Hao Zhang. 2019. Learning implicit fields for generative shape modeling. In *Proceedings of the IEEE/CVF conference on computer vision and pattern recognition*. 5939–5948.

[Clémot and Digne(2023)] Mattéo Clémot and Julie Digne. 2023. Neural skeleton: Implicit neural representation away from the surface. *Computers & Graphics* 114 (2023), 368–378.

[Culver et al.(1999)] Tim Culver, John Keyser, and Dinesh Manocha. 1999. Accurate computation of the medial axis of a polyhedron. In *Proceedings of the fifth ACM symposium on Solid modeling and applications*. 179–190.

[Culver et al.(2004)] Tim Culver, John Keyser, and Dinesh Manocha. 2004. Exact computation of the medial axis of a polyhedron. *Computer Aided Geometric Design* 21, 1 (2004), 65–98.

[Dey and Zhao(2004)] Tamal K Dey and Wulue Zhao. 2004. Approximating the medial axis from the Voronoi diagram with a convergence guarantee. *Algorithmica* 38 (2004), 179–200.

[Dou et al.(2022)] Zhiyang Dou, Cheng Lin, Rui Xu, Lei Yang, Shiqing Xin, Taku Komura, and Wenping Wang. 2022. Coverage axis: Inner point selection for 3d shape skeletonization. In *Computer Graphics Forum*, Vol. 41. Wiley Online Library, 419–432.

[Dou et al.(2023)] Zhiyang Dou, Qingxuan Wu, Cheng Lin, Zeyu Cao, Qiangqiang Wu, Weilin Wan, Taku Komura, and Wenping Wang. 2023. Tore: Token reduction for efficient human mesh recovery with transformer. In *Proceedings of the IEEE/CVF International Conference on Computer Vision*. 15143–15155.

[Garland and Heckbert(1997)] Michael Garland and Paul S Heckbert. 1997. Surface simplification using quadric error metrics. In *Proceedings of the 24th annual conference on Computer graphics and interactive techniques*. 209–216.

[Ge et al.(2023)] Mengyuan Ge, Junfeng Yao, Baorong Yang, Ningna Wang, Zhonggui Chen, and Xiaohu Guo. 2023. Point2MM: Learning medial mesh from point clouds. *Computers & Graphics* 115 (2023), 511–521.

[Giesen et al.(2006)] Joachim Giesen, Edgar A Ramos, and Bardia Sadri. 2006. Medial axis approximation and unstable flow complex. In *Proceedings of the twenty-second annual symposium on Computational geometry*. 327–336.

[Hesselink and Roerdink(2008)] Wim H Hesselink and Jos BTM Roerdink. 2008. Euclidean skeletons of digital image and volume data in linear time by the integer medial axis transform. *IEEE Transactions on Pattern Analysis and Machine Intelligence* 30, 12 (2008), 2204–2217.

[Hou et al.(2023)] Fei Hou, Xuhui Chen, Wencheng Wang, Hong Qin, and Ying He. 2023. Robust zero level-set extraction from unsigned distance fields based on double covering. *ACM Transactions on Graphics (TOG)* 42, 6 (2023), 1–15.

[Huang et al.(2019)] Zhiyang Huang, Nathan Carr, and Tao Ju. 2019. Variational implicit point set surfaces. *ACM Transactions on Graphics (TOG)* 38, 4 (2019), 1–13.

[Huang et al.(2024)] Zhangjin Huang, Yuxin Wen, Zihao Wang, Jinjuan Ren, and Kui Jia. 2024. Surface reconstruction from point clouds: A survey and a benchmark. *IEEE Transactions on Pattern Analysis and Machine Intelligence* (2024).

[Jalba et al.(2012)] Andrei C Jalba, Jacek Kustra, and Alexandru C Telea. 2012. Surface and curve skeletonization of large 3D models on the GPU. *IEEE transactions on pattern analysis and machine intelligence* 35, 6 (2012), 1495–1508.

[Kazhdan and Hoppe(2013)] Michael Kazhdan and Hugues Hoppe. 2013. Screened poisson surface reconstruction. *ACM Trans. Graph.* 32, 3, Article 29 (July 2013), 13 pages. <https://doi.org/10.1145/2487228.2487237>

[Koch et al.(2019)] Sebastian Koch, Albert Matveev, Zhongshi Jiang, Francis Williams, Alexey Artemov, Evgeny Burnaev, Marc Alexa, Denis Zorin, and Daniele Panozzo. 2019. Abc: A big cad model dataset for geometric deep learning. In *Proceedings of the IEEE/CVF conference on computer vision and pattern recognition*. 9601–9611.

[Lan et al.(2020)] Lei Lan, Ran Luo, Marco Fratarcangeli, Wei-wei Xu, Huamin Wang, Xiaohu Guo, Junfeng Yao, and Yin Yang. 2020. Medial elastics: Efficient and collision-ready deformation via medial axis transform. *ACM Transactions on Graphics (TOG)* 39, 3 (2020), 1–17.

[Lan et al.(2021)] Lei Lan, Yin Yang, Danny Kaufman, Junfeng Yao, Minchen Li, and Chenfanfu Jiang. 2021. Medial IPC: accelerated incremental potential contact with medial elastics. *ACM Transactions on Graphics* 40, 4 (2021).

[Li et al.(2015)] Pan Li, Bin Wang, Feng Sun, Xiaohu Guo, Caiming Zhang, and Wenping Wang. 2015. Q-mat: Computing medial axis transform by quadratic error minimization. *ACM Transactions on Graphics (TOG)* 35, 1 (2015), 1–16.

[Lin et al.(2021)] Cheng Lin, Changjian Li, Yuan Liu, Nenglun Chen, Yi-King Choi, and Wenping Wang. 2021. Point2skeleton: Learning skeletal representations from point clouds. In *Proceedings of the IEEE/CVF conference on computer vision and pattern recognition*. 4277–4286.

[Lin et al.(2020)] Cheng Lin, Lingjie Liu, Changjian Li, Leif Kobbelt, Bin Wang, Shiqing Xin, and Wenping Wang. 2020. Seg-mat: 3d shape segmentation using medial axis transform. *IEEE transactions on visualization and computer graphics* 28, 6 (2020), 2430–2444.

[Lorensen and Cline(1998)] William E Lorensen and Harvey E Cline. 1998. Marching cubes: A high resolution 3D surface construction algorithm. In *Seminal graphics: pioneering efforts that shaped the field*. 347–353.

[Ma et al.(2012)] Jaehwan Ma, Sang Won Bae, and Sunghee Choi. 2012. 3D medial axis point approximation using nearest neighbors and the normal field. *The Visual Computer* 28 (2012), 7–19.

[Miklos et al.(2010)] Balint Miklos, Joachim Giesen, and Mark Pauly. 2010. Discrete scale axis representations for 3D geometry. In *ACM SIGGRAPH 2010 papers*. 1–10.

[Milenkovic(1993)] Victor Milenkovic. 1993. Robust Construction of the Voronoi Diagram of a Polyhedron.. In *CCCG*, Vol. 93. Citeseer, 473–478.

[Noma et al.(2024)] Yuta Noma, Silvia Sellán, Nicholas Sharp, Karan Singh, and Alec Jacobson. 2024. Surface-Filling Curve Flows via Implicit Medial Axes. *ACM Transactions on Graphics (TOG)* 43, 4 (2024), 1–12.

[Palágyi and Kuba(1999)] Kálmán Palágyi and Attila Kuba. 1999. A parallel 3D 12-subiteration thinning algorithm. *Graphical Models and Image Processing* 61, 4 (1999), 199–221.

[Pan et al.(2019)] Yiling Pan, Bin Wang, Xiaohu Guo, Hua Zeng, Yuexin Ma, and Wenping Wang. 2019. Q-MAT+: An error-controllable and feature-sensitive simplification algorithm for medial axis transform. *Computer Aided Geometric Design* 71 (2019), 16–29.

[Park et al.(2019)] Jeong Joon Park, Peter Florence, Julian Straub, Richard Newcombe, and Steven Lovegrove. 2019. Deepsdf: Learning continuous signed distance functions for shape representation. In *Proceedings of the IEEE/CVF conference on computer vision and pattern recognition*. 165–174.

[Petrov et al.(2024)] Dmitry Petrov, Pradyumn Goyal, Vikas Thamizharasan, Vladimir Kim, Matheus Gadelha, Melinos Averkiou, Siddhartha Chaudhuri, and Evangelos Kalogerakis. 2024. GEM3D: GEnerative Medial Abstractions for 3D Shape Synthesis. In *ACM SIGGRAPH 2024 Conference Papers*. 1–11.

[Pudney(1998)] Chris Pudney. 1998. Distance-ordered homotopic thinning: a skeletonization algorithm for 3D digital images. *Computer vision and image understanding* 72, 3 (1998), 404–413.

[Ramanathan and Gurumoorthy(2010)] M Ramanathan and B Gurumoorthy. 2010. Interior medial axis transform computation of 3D objects bound by free-form surfaces. *Computer-Aided Design* 42, 12 (2010), 1217–1231.

[Rebain et al.(2021)] Daniel Rebain, Ke Li, Vincent Sitzmann, Soroosh Yazdani, Kwang Moo Yi, and Andrea Tagliasacchi. 2021. Deep medial fields. *arXiv preprint arXiv:2106.03804* (2021).

[Rumpf and Telea(2002)] Martin Rumpf and Alexandru Telea. 2002. A continuous skeletonization method based on level sets. In *EPRINTS-BOOK-TITLE*. University of Groningen, Johann Bernoulli Institute for Mathematics and ....

[Saha et al.(2016)] Punam K Saha, Gunilla Borgefors, and Gabriella Sanniti di Baja. 2016. A survey on skeletonization algorithms and their applications. *Pattern recognition letters* 76 (2016), 3–12.

[Sherbrooke et al.(1996)] Evan C Sherbrooke, Nicholas M Patrikalakis, and Erik Brisson. 1996. An algorithm for the medial axis transform of 3D polyhedral solids. *IEEE transactions on visualization and computer graphics* 2, 1 (1996), 44–61.

[Tagliasacchi et al.(2016)] Andrea Tagliasacchi, Thomas Delame, Michela Spagnuolo, Nina Amenta, and Alexandru Telea. 2016. 3d skeletons: A state-of-the-art report. In

*Computer Graphics Forum*, Vol. 35. Wiley Online Library, 573–597.

[Tang et al.(2019)] Jiapeng Tang, Xiaoguang Han, Junyi Pan, Kui Jia, and Xin Tong. 2019. A skeleton-bridged deep learning approach for generating meshes of complex topologies from single rgb images. In *Proceedings of the ieee/cvf conference on computer vision and pattern recognition*. 4541–4550.

[Wang et al.(2024b)] Ningna Wang, Hui Huang, Shibo Song, Bin Wang, Wenping Wang, and Xiaohu Guo. 2024b. MATTOP: Topology-preserving Medial Axis Transform with Restricted Power Diagram. *arXiv preprint arXiv:2403.18761* (2024).

[Wang et al.(2022)] Ningna Wang, Bin Wang, Wenping Wang, and Xiaohu Guo. 2022. Computing medial axis transform with feature preservation via restricted power diagram. *ACM Transactions on Graphics (TOG)* 41, 6 (2022), 1–18.

[Wang et al.(2024a)] Zimeng Wang, Zhiyang Dou, Rui Xu, Cheng Lin, Yuan Liu, Xiaoxiao Long, Shiqing Xin, Taku Komura, Xiaoming Yuan, and Wenping Wang. 2024a. Coverage Axis++: Efficient Inner Point Selection for 3D Shape Skeletonization. In *Computer Graphics Forum*. Wiley Online Library, e15143.

[Wu et al.(2015)] Shihao Wu, Hui Huang, Minglun Gong, Matthias Zwicker, and Daniel Cohen-Or. 2015. Deep Points Consolidation. *ACM Transactions on Graphics (Proc. of SIGGRAPH Asia)* 34, 6 (2015), 176:1–176:13.

[Yan et al.(2018)] Yajie Yan, David Letscher, and Tao Ju. 2018. Voxel cores: Efficient, robust, and provably good approximation of 3d medial axes. *ACM Transactions on Graphics (TOG)* 37, 4 (2018), 1–13.

[Yang et al.(2018)] Baorong Yang, Junfeng Yao, and Xiaohu Guo. 2018. DMAT: Deformable medial axis transform for animated mesh approximation. In *Computer Graphics Forum*, Vol. 37. Wiley Online Library, 301–311.

[Yang et al.(2020)] Baorong Yang, Junfeng Yao, Bin Wang, Jianwei Hu, Yiling Pan, Tianxiang Pan, Wenping Wang, and Xiaohu Guo. 2020. P2MAT-NET: Learning medial axis transform from sparse point clouds. *Computer Aided Geometric Design* 80 (2020), 101874.

[Yang et al.(2021)] Yiding Yang, Zhou Ren, Haoxiang Li, Chunluan Zhou, Xinchao Wang, and Gang Hua. 2021. Learning dynamics via graph neural networks for human pose estimation and tracking. In *Proceedings of the IEEE/CVF conference on computer vision and pattern recognition*. 8074–8084.

[Zhou and Jacobson(2016)] Qingnan Zhou and Alec Jacobson. 2016. Thingi10k: A dataset of 10,000 3d-printing models. *arXiv preprint arXiv:1605.04797* (2016).

[Zhou et al.(2015)] Yang Zhou, Kangxue Yin, Hui Huang, Hao Zhang, Minglun Gong, and Daniel Cohen-Or. 2015. Generalized cylinder decomposition. *ACM Trans. Graph.* 34, 6 (2015), 171–1.